Journal of Materials Chemistry C

ROYAL SOCIETY OF CHEMISTRY

PAPER

View Article Online
View Journal | View Issue

Check for updates

Cite this: J. Mater. Chem. C, 2025, 13, 6736

Conductive network enhanced self-assembled diphasic Prussian blue analogs for aqueous zinc-ion batteries†

Bingbing Hu, ‡*[a] Dongshan Li,‡[a] Meixin Li,[a] Jiayu Jiang,[a] Ye Zou,[a] Yu Deng,[a] Zideng Zhou,[a] Hong Pu,[b] Guangqiang Ma[b] and Zhi Li *[a]

Zinc hexacyanoate (ZnHCF), one of the Prussian blue analogs (PBAs), is a promising cathode material for rechargeable aqueous batteries due to its easy synthesis and open framework. However, the low-capacity problem limits its further development. In this work, a low-cost and simple hydrothermal method is used to grow a diphasic Prussian blue composite material (ZnVHCF) on reduced graphene oxide (rGO), aiming to improve the specific capacity and conductivity of the electrode material by introducing vanadium-based Prussian blue and rGO conductive networks. Meanwhile, the electrolyte additive is utilized as a strategy to suppress the vanadium dissolution of cathode materials. Based on the synergistic effect of multiple strategies, the reduced graphene oxide modified vanadium–zinc diphasic Prussian blue (ZnVHCF@rGO) composite material exhibits excellent zinc storage performance. It shows a higher specific capacity of 152.3 mA h g^{-1} at a current density of 0.1 A g^{-1}. In addition, the VO^{2+} sol–gel electrolyte additive provides additional capacity due to the electrochemical activity of V and delays material dissolution based on the principle of solvation equilibrium. The capacity reaches 84.1 mA h g^{-1} at a current of 5 A g^{-1}, which is an improvement of 26.1%. And the cycling stability is improved by 25.2% after 300 cycles. This work provides new ideas for the design of high-performance PBA cathodes for AZIBs.

Received 7th December 2024,
Accepted 10th February 2025

DOI: 10.1039/d4tc05159a

rsc.li/materials-c

Published on 13 February 2025. Downloaded on 1/18/2026 11:00:12 PM.

1. Introduction

With the excessive consumption of non-renewable fossil fuels and global warming, it is important to develop green and efficient energy storage technologies.[1–4] Aqueous zinc-ion batteries (AZIBs) have attracted much attention due to the unparalleled advantages of the aqueous electrolyte and zinc anode.[5] Specifically, aqueous electrolytes have high ionic conductivity, low cost, and non-flammability compared to organic electrolytes.[6,7] In addition, zinc anodes are abundant, nontoxic, and low cost. And they have a low redox potential (−0.76 V *vs.* SHE) and high specific capacity (820 mA h g^{-1}),[8–10] with good reversibility in aqueous electrolytes.[11] However, their low energy density limits their application scenarios. The search for suitable cathode materials with high voltage and high capacity is very urgent.[12] Among the many cathode materials,[13–16] Prussian blue analogs (PBAs) materials have been widely studied due to their open framework with wide adaptability to various carrier ions.[17,18]

Zinc hexacyanoferrate (ZnHCF), one of PBAs, is a promising cathode material for rechargeable aqueous batteries.[19,20] Liu[21] *et al.* first proposed AZIBs using the rhombohedral $Zn_3[Fe(CN)_6]_2$ (ZnHCF) cathode, which exhibited a low capacity of 65.4 mA h g^{-1} after 100 cycles with 76% capacity retention. The low capacity is due to the electrochemical inactivity of Zn. During electrochemical charging and discharging, Zn^{2+} does not participate in redox reactions, so there is only one charging/discharging plateau or anode/cathode peak induced electron transfer (Fe^{2+}–Fe^{3+}).[22] Based on this fact, a diphasic Prussian blue analog is proposed. It is obtained by utilizing a vanadium-based Prussian blue material with multi-electron transfer to modify the ZnHCF.[23,24] The performance coupling of the diphasic Prussian blue analogs further increases the specific capacity of PBAs. However, the electrochemical stability of PBAs in aqueous media is poor, and one strategy to overcome this problem is the preparation of carbon/Prussian blue composites with reduced graphene oxide (rGO) and carbon nanotubes (CNTs).[24–26] The use of carbon materials can provide excellent conductive structures, which are important

[a] China-Spain Collaborative Research Center for Advanced Materials, College of Materials Science and Engineering, Chongqing Jiaotong University, Chongqing, 400074, China. E-mail: hubingbing@cqjtu.edu.cn
[b] Sichuan Vanadium Titanium Materials Engineering Technology Research Center, Panzhihua University, Panzhihua, 617000, Sichuan, China

† Electronic supplementary information (ESI) available. See DOI: https://doi.org/10.1039/d4tc05159a

‡ These authors have contributed equally.

This journal is © The Royal Society of Chemistry 2025

Published on 13 February 2025. Downloaded on 1/18/2026 11:00:12 PM.

for their electrochemical performance.[27,28] In particular, graphene has a two-dimensional conductive plane made up of large π-bonds, and functional groups can be freely added to enrich interfacial effects.[29] Graphene-based materials can be used in energy storage devices, especially because of their impressive electrical conductivity.[30,31] Therefore, the introduction of graphene can further improve the electrochemical properties of the diphasic Prussian blue material and increase the electrical conductivity, as well as protect the material from direct contact with the active water molecules in the electrolyte and delay the dissolution process of the material.

In addition, vanadium-based materials inevitably suffer from vanadium dissolution. This can lead to the structural collapse of vanadium-based Prussian blue, affecting the coupling of diphasic Prussian blue. In the electrolyte, in order to decrease the dissolution of materials, researchers have utilized a highly concentrated "water in salt"(WIS) electrolyte to reduce the water content and tune the solvation structure of the electrolyte.[32,33] Liu[34] *et al.* introduced a certain amount of LiOTF and designed an electrolyte of 2 M $Zn(OTF)_2$ + 8 M LiOTF, which effectively reduces the number of free water molecules. It also inhibits the activity of water molecules and improves the stability of the electrode/electrolyte interface, improving the cycling stability of VO_2 effectively. Although the performance of "WIS" electrolytes has improved, their practical application is still hampered by high cost, increased viscosity, less ionic conductivity, and low energy density due to the increase in salt concentration.[35] Based on the vanadium oxide dissolution equilibrium principle, it is possible to inhibit the dissolution of elemental vanadium by adding appropriate vanadium sols into the aqueous electrolyte. In addition, vanadium sols can provide additional capacity during charging and discharging due to the redox activity of V.[36]

To overcome the above issues, this study proposes a reduced graphene oxide reinforced diphasic Prussian blue composite cathode material (ZnVHCF@rGO) and vanadium sol as the electrolyte modifier. The comprehensive performance of zinc-ion batteries is improved using multiple strategies and has the following advantages: (1) zinc powder is used as the reducing agent to obtain low valence vanadium solution, which is the precursor solution. The diphasic Prussian blue (ZnVHCF) composite is obtained *via* a hydrothermal method with a simple preparation process and low cost; (2) the electrochemical performance of ZnVHCF is enhanced by the introduction of reduced graphene oxide *via* the hydrothermal method. The electrical conductivity is improved, and direct contact between the material and the active water in the electrolyte is avoided, thus delaying the dissolution of the material. (3) Based on the principle of solvation equilibrium, the electrolyte employed is 3 M Zn $(CF_3SO_3)_2$ + 0.1 M VO^{2+}. It inhibits the vanadium dissolution of ZnVHCF@rGO and the vanadium sol provides additional capacity due to the redox activity of V. Compared to ZnHCF, the experimental results show that the diphasic Prussian blue (ZnVHCF) has a higher specific capacity with 96.7 mA h g^{-1} at a current of 0.1 A g^{-1}. With the introduction of rGO, more favorable electrochemical performance is achieved for ZnVHCF@rGO, reaching 152.3 mA h g^{-1} at 0.1 A g^{-1}. And it has higher electrical conductivity and ion diffusion ability. In addition, the VO^{2+} sol–gel electrolyte additive provides additional capacity and retards the dissolution of the material, improving capacity by 27.3% at 5 A g^{-1} reaching 84.1 mA h g^{-1} and cycle stability by 25.2% after 300 cycles.

2. Experimental

2.1 Materials

All the chemicals utilized in the study are sourced from Shanghai Aladdin Biochemical Technology.

2.2 Material preparation

2.2.1 Preparation of ZnHCF. 2 mmol $ZnSO_4$ and 2 mmol $K_3Fe(CN)_6$ are dissolved in 20 ml of deionized water with stirring, and then the $K_3Fe(CN)_6$ solution is slowly dripped into the $ZnSO_4$ solution with a hydrothermal method at 150 °C for 8 h. The product is dried in a vacuum drying oven at 60 °C for 12 h after filtering and washing, and ZnHCF is obtained.

2.2.2 Preparation of ZnVHCF and ZnVHCF@rGO. 2 mmol V_2O_5 is dissolved in 38 ml water mixed with 2 ml H_2O_2. Subsequently, excess of zinc powder is added and the residue is filtered out after obtaining a dark green color solution; the green color solution obtained is recorded as liquid A. Then, 4 mmol $K_3Fe(CN)_6$ is dissolved in 40 ml of deionized water, which is recorded as liquid B. Finally, liquid B is slowly dripped into liquid A and synthesized *via* a hydrothermal method at 150 °C for 8 h. The product is filtered and washed, then dried in a vacuum oven at 60 °C for 12 h to obtain ZnVHCF. In particular, the hydrothermal product with 3 mg ml^{-1} of graphene dispersion in liquid A is denoted as ZnVHCF@rGO.

2.2.3 Preparation of the electrolyte. The modified electrolyte is obtained by mixing 3 M Zn $(CF_3SO_3)_2$ and 0.1 M VO^{2+} in a one-to-one ratio by volume.

2.3 Material characterization

A scanning electron microscope (SEM, ZEISS Sigma 300) and a transmission electron microscope (TEM, FEI Tecnai F20) are employed to observe the morphology, size and microstructure of the materials. The X-ray diffraction (XRD) patterns of the materials are obtained by using a Rigaku XRD-6100 ray diffractometer. Fourier transform infrared spectroscopy (FT-IR) analysis is performed using a Thermo Fisher Nicolet IS20 infrared spectrometer. The Raman spectra are obtained using a HORIBA Xplora Plus, Japan. Thermogravimetric analysis is carried out using an integrated thermal analyzer (NETZSCH TG 209F3) under an air atmosphere and the heating rate is 10 °C min^{-1}. X-ray photoelectron spectroscopy (XPS) tests are performed using a Thermo Scientific K-Alpha with Al Kα X-rays.

2.4 Electrochemical testing

The active material (synthetic samples), super-p and PVDF are milled in a quality ratio of 7 : 2 : 1, and then dispersed into NMP. A stainless steel mesh is used as a substrate to uniformly coat the resulting slurry and then heated in a vacuum oven at

Published on 13 February 2025. Downloaded on 1/18/2026 11:00:12 PM.

60 °C for 12 h, and the quantity of the active material deposited on the stainless-steel mesh is 1.5 mg cm^{-2}. The synthetic material acts as the cathode, the zinc metal foil is used as the anode, the 3 M $Zn(CF_3SO_3)_2$ is used as the electrolyte, and the separator is formed by glass fibers (Olegeeino GF/D) to assemble CR2032 coin cells under an air atmosphere. Cyclic voltammogram (CV) tests are conducted using a Koester electrochemical workstation, operating within a voltage window between 0.2 and 2.0 V. Constant-current charge/discharge (GCD) tests and constant-current intermittent titration (GITT) tests of the assembled coin cell are performed on a NEWARE-BTS-3008 battery test system in the equal voltage window.

3. Results and discussion

3.1 Characterization of materials

The preparation schematic diagram of ZnVHCF@rGO is shown in Fig. 1. Firstly, the excess zinc powder as a reductant is added into the V_2O_5 solution and stirred to obtain a green solution, and then the GO dispersion is added. Full ultrasonication and stirring are performed to obtain a uniform dispersion. The positively charged V^{3+} and Zn^{2+} ions are electrostatically self-assembled on negatively charged GO. Then, $K_3[Fe(CN)_6]$ is introduced into the above mixture via the hydrothermal method. ZnVHCF nanoparticles are *in situ* grown on the rGO. Finally, the product is obtained by washing and drying.

The micro-morphology of the material is characterized by SEM and TEM. As shown in Fig. 2a, ZnHCF exhibits a typical Prussian blue cubic structure with a size around 200–400 nm.[37] The diphasic Prussian blue ZnVHCF shows a smoother surface (Fig. 2b), while a layer of VHCF grows on the surface of ZnHCF. And the VHCF is composed of nano-particles with a size of about 20–30 nm, which is the same as the SEM image of the VHCF (Fig. S1, ESI†). The presence of VHCF provides additional active sites and could increase the capacity. The ZnVHCF@rGO image is shown in Fig. 2c, and it can be observed that rGO and ZnVHCF form a cross-linked network. TEM images show that ZnVHCF particles have uniform and well-anchored growth on rGO sheets, forming well-crosslinked structures (Fig. 2c–f). The introduction of rGO will reduce the resistance of the material and enhance the kinetics of electric transfer.[38] Furthermore, the EDS images in Fig. 2g and Fig. S2 (ESI†) are analyzed and found to have Zn, V, Fe, C, N and O elements with uniform distribution, indicating the successful preparation of the material.

The XRD image of ZnVHCF is shown in Fig. 3a, which indicates that it has a typical Prussian blue cubic structure, and the diffraction peaks can be seen to be highly overlapping with the face-centered cubic $V_{1.5}Fe(CN)_6$[39] and $K_2Zn_3(Fe(CN)_6)_2 \cdot 9H_2O$.[40] The introduction of rGO will not change the crystal structure of ZnVHCF. Fig. 3b demonstrates the FT-IR images of ZnHCF, ZnVHCF and ZnVHCF@rGO, and there is no obvious difference between the three samples. In particular, the absorption peaks at 3433 cm^{-1} and 1634 cm^{-1} are attributed to H–O–H bending and O–H stretching modes, respectively, confirming the presence of adsorbed water and crystal water.[41] The absorption peak at 2094 cm^{-1} corresponds to the C≡N stretching vibration.[42] The peaks at 494 cm^{-1} and 596 cm^{-1} are respectively due to Fe–CN–M bending and Fe–CN vibrations.[43] In contrast to ZnHCF, ZnVHCF and ZnVHCF@rGO show absorption peaks at 967 cm^{-1} attributed to V=O.[44] Fig. 3c shows the Raman spectrum of ZnVHCF@rGO and graphene. It shows two peaks at 1354 cm^{-1} and 1586 cm^{-1}, which can be attributed to the D and G bands of the carbonaceous material, respectively.[45] Compared to the GO, ZnVHCF@rGO has a lower I_D/I_G value (0.97), indicating that the material has higher extent of graphitization by using the hydrothermal method, which ensures fast electron transport and improves the electrochemical properties of materials.[46,47] As shown in Fig. S3 (ESI†), thermogravimetric (TG) tests are carried out on the material to determine the content of rGO, and the weight loss below 200° can be attributed to the evaporation of adsorbed water and crystal water from the material. And the subsequent weight loss is attributed to the decomposition of the material and rGO. By comparing the two TG curves, it can be determined that the rGO content in the material is approximately 8.93%.

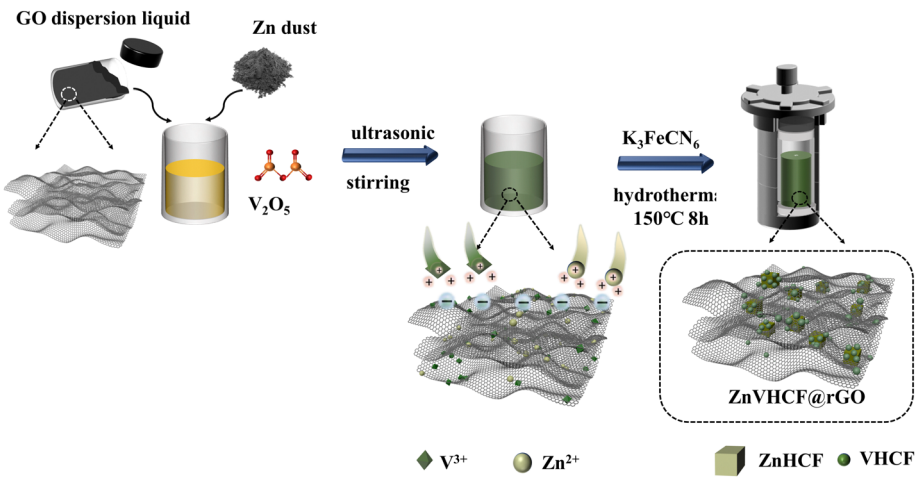

Fig. 1 Diagram of the cathode material preparation process.

 This journal is © The Royal Society of Chemistry 2025

Published on 13 February 2025. Downloaded on 1/18/2026 11:00:12 PM.

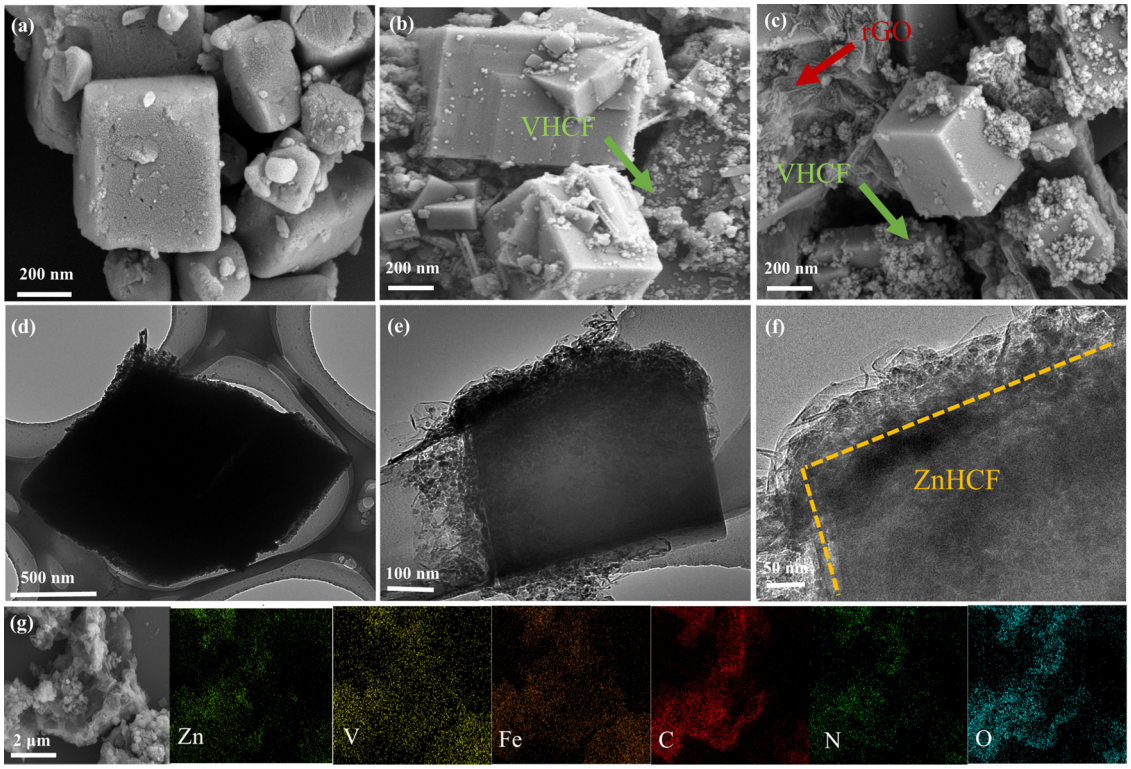

Fig. 2 SEM images of (a) ZnHCF, (b) ZnVHCF, and (c) ZnVHCF@rGO, (d)–(f) TEM images, and (g) EDS pattern of ZnVHCF@rGO.

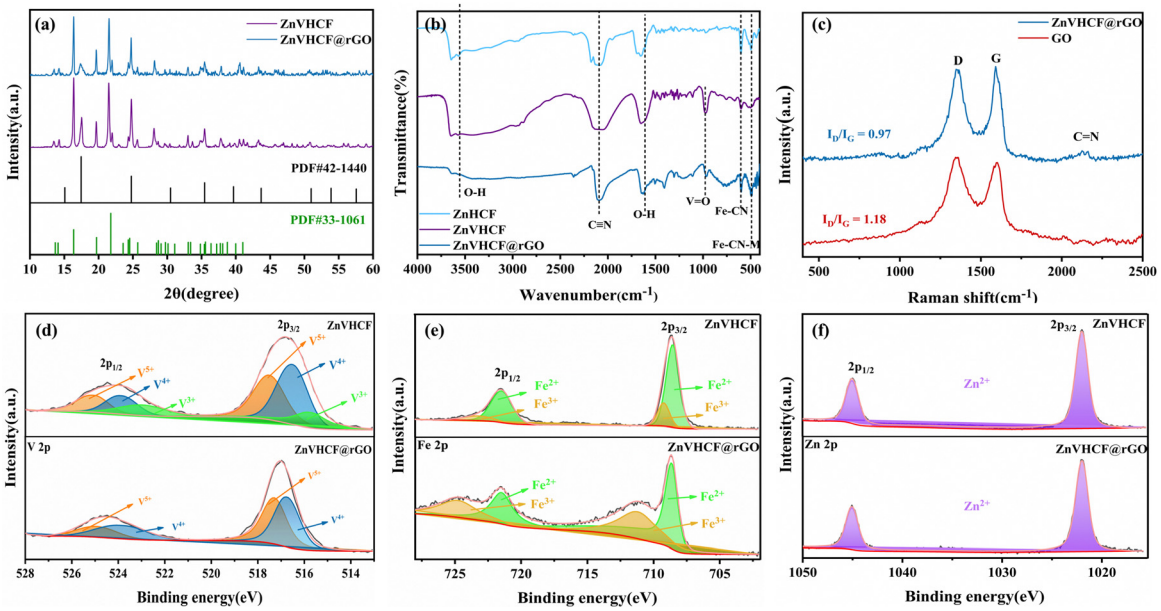

Fig. 3 (a) XRD patterns of ZnVHCF and ZnVHCF@rGO; (b) FT-IR spectra of ZnHCF, ZnVHCF and ZnVHCF@rGO; (c) Raman spectrum of ZnVHCF@rGO and rGO; high-resolution XPS spectra of (d) V 2P and (e) Fe 2p and (f) Zn 2p for ZnVHCF and ZnVHCF@rGO.

Furthermore, X-ray photoelectron spectroscopy (XPS) is used to determine the elemental composition and chemical state of the prepared materials, identifying the presence of elements such as Zn, Fe, O, N, K, and C in ZnVHCF and ZnVHCF@rGO (Fig. S4, ESI†). Fig. 3d shows the presence of two peak pairs in the high resolution V 2p spectra. Specifically, for ZnVHCF, the peaks V $2p_{1/2}$ and V $2p_{3/2}$ are attributed to V^{3+} (522.8 eV/515.6 eV), V^{4+} (523.5 eV/516.3 eV) and V^{5+} (525.2 eV/517.6 eV),

Published on 13 February 2025. Downloaded on 1/18/2026 11:00:12 PM.

respectively.[48] In addition, the two pairs of peaks in the Fe 2p spectrum decompose into 721.5 eV/708.4 eV and 723.6 eV/709.2 eV, corresponding to Fe^{2+} and Fe^{3+} respectively[24] (Fig. 3e). Moreover, there reveal two different peaks at 1021.9 eV and 1045.1 eV, corresponding to Zn $2p_{3/2}$ *versus* Zn $2p_{1/2}$ as shown in Fig. 3f.[36] Compared to ZnVHCF, V^{3+} is not detected and the Fe^{3+} content is higher in ZnVHCF@rGO, which may be due to the reduction of GO during the hydrothermal process leading to oxidation of some V^{3+} with Fe^{2+}. In addition, there is a tiny shift in the binding energy of V and Fe in ZnVHCF@rGO, which may be caused by the charge transfer because of the introduction of rGO.

3.2 Electrochemical performance

The electrochemical performance of materials is tested by assembling them into coin-type batteries and the electrolyte is 3 M $Zn(CF_3SO_3)_2$. As shown in Fig. S5a and b (ESI†), the diphasic Prussian blue ZnVHCF has multiple redox peaks and charge/discharge platforms, which is due to the introduction of vanadium to provide multiple electron transfer. It can make up for the low capacity caused by the single electron transfer of ZnHCF. Fig. 4a demonstrates the CV images of ZnVHCF and ZnVHCF@rGO, which can be clearly observed to have four pairs of redox peaks. For ZnVHCF@rGO, the 1.12/0.91 V and 0.73/0.54 V pairs can be assigned to the V^{5+}/V^{4+} and V^{4+}/V^{3+} redox pairs, respectively, while the 1.84/1.71 V pair can be attributed to the Fe^{3+}/Fe^{2+},[24] which is the same as in the GCD charge/discharge platform. And the redox pairs at 1.12/0.91 V may correspond to the de/insertion of H^+. Compared to ZnVHCF, ZnVHCF@rGO has a larger peak current, which is due to the introduction of rGO. It increases the conductivity and improves the electrochemical activity of the material. Additionally, this multi-electronic redox reaction leads to multiple voltage plateaus that can take full advantage of the crystal structure for storage of inserted ions.[22] Electrochemical test results show that the diphasic Prussian blue ZnVHCF reaches a capacity of 96.7 mA h g^{-1} at a current density of 0.1 A g^{-1}, while ZnHCF reaches a capacity of only 62.4 mA h g^{-1} (Fig. S5b, ESI†). This is due to the presence of vanadium, which exhibits excellent electrochemical activity and it could achieve multi-electron transfer during redox reactions to enhance the specific capacity.[49] After the introduction of VHCF, V serves as an active site, providing additional capacity for the ZnHCF phase and significantly improving the overall performance of the composite of ZnVHCF. In addition, ZnVHCF@rGO shows a higher specific capacity of 152.3 mA h g^{-1} at 0.1 A g^{-1} (Fig. 4b). This is mainly attributed to the crosslinked conducting network structure formed by rGO and ZnVHCF, which provides good electron transfer pathways and activates abundant carrier insertion active sites,[50] enhancing the electrochemical performance of the material. Additionally, to further suppress the vanadium dissolution problem in aqueous electrolytes, a synergistic modification of the electrolyte based on the principle of dissolution equilibrium is performed. Specifically, the use of vanadium solutes (VO^{2+}) as electrolyte additives can counteract vanadium dissolution.[36] As shown in Fig. S5c and d (ESI†), it can be observed that the introduction of the VO^{2+} additive enhances

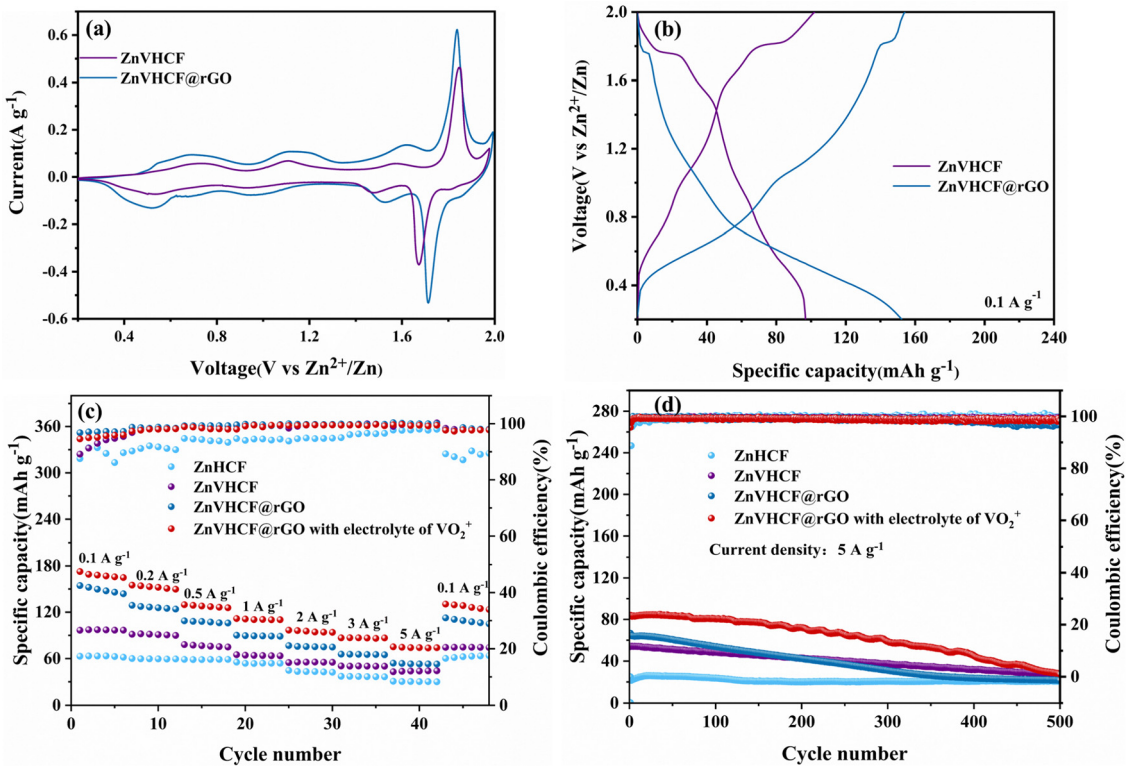

Fig. 4 (a) CV curves at 0.2 mV s^{-1} and (b) GCD curves at 0.1 A g^{-1} of ZnVHCF and ZnVHCF@rGO; (c) rate capability and (d) long-cycle performance under 5 A g^{-1} of materials.

 This journal is © The Royal Society of Chemistry 2025

Published on 13 February 2025. Downloaded on 1/18/2026 11:00:12 PM.

the peak of the V redox pair and improves the electrochemical activity and capacity (166.8 mA h g^{-1} at 0.1 A g^{-1}). And the polarization is smaller, suggesting better reaction kinetics in the electrolyte of 3 M Zn $(CF_3SO_3)_2$ + 0.1 M VO^{2+}. In order to examine the effect of VO^{2+} sol introduction in the electrolyte on the ZnHCF phase, the CV curves of ZnHCF are obtained in the two electrolytes, respectively (Fig. S6, ESI†). It can be seen that the electrolyte containing 3 M Zn $(CF_3SO_3)_2$ + 0.1 M VO^{2+} exhibits more peaks compared with the electrolyte containing 3 M Zn $(CF_3SO_3)_2$. This could enable more electron transfer and additional capacity due to the electrochemical activity of VO^{2+}. These findings are consistent with the results obtained for ZnVHCF@rGO in both electrolytes (Fig. S5c, ESI†). This indicates that the presence of VO^{2+} does not influence the ZnHCF phase, while it enhances the reactivity of V in VHCF and contributes additional capacity due to its intrinsic electrochemical activity.

The rate capability of the material is shown in Fig. 4c. With the rise of current density from 0.1 to 5 A g^{-1}, the average discharging capacities of ZnVHCF@rGO are 150.1, 126.7, 108.2, 89.4, 75.5, 65.4 and 54.1 mA h g^{-1} for 0.1, 0.2, 0.5, 1, 2, 3 and 5 A g^{-1}, respectively. It is superior to both ZnVHCF and ZnHCF. In addition, vanadium sol (VO^{2+}) as an electrolyte additive demonstrated a higher specific capacity under the same conditions. These results indicate that the introduction of rGO and the VO^{2+} additive makes the material have good multiplicative properties and provides additional capacity. Long cycle tests of materials at 5 A g^{-1} are illustrated in Fig. 4d. The initial capacity of the ZnVHCF@rGO is 66.7 mA h g^{-1}, and after 300 cycles it is 32.3 mA h g^{-1}, with a capacity retention rate of only 46.9%. The introduction of vanadium sol (VO^{2+}) as an electrolyte additive increased the capacity retention rate at 72.1% under the same conditions, which is improved by 25.2%. The above results prove that the VO^{2+} electrolyte additive can inhibit the effect of vanadium dissolution on the performance and improve the cycling stability of the material. Additionally, the near-100% coulombic efficiency reflects the high invertibility of the charging and discharging reactions.

In order to investigate the electrochemical kinetics of ZnVHCF@rGO in the 3 M Zn $(CF_3SO_3)_2$ + 0.1 M VO^{2+} electrolyte, its plotted CV curves at different scan rates are shown in Fig. 5a. The peak current (i) and scan rate (v) usually satisfy the equation $i = av^b$, where a and b are variables. b values close to 0.5 indicate that the reaction process is mainly controlled by the diffusion of ions, while b equal to 1 indicates the predominant capacitive behavior.[51] As shown in Fig. 5b, the b-values obtained from the fitting of the three pairs of redox peaks are 0.63/0.58/0.63/0.91/0.71.0.69, which implies that ZnVHCF@rGO is in synergy controlled by both diffusive and capacitive behaviors, with capacitive behavior dominating the electrode kinetics. In addition, the pseudocapacitive contribution to the capacity is further calculated using the equation $i = k_1v + k_2v^{1/2}$, where k_1v denotes pseudocapacitive behavior and $k_2v^{1/2}$ denotes diffusive behavior.[52] The results are shown in Fig. 5c, from which it can be observed that the pseudo capacitance contribution reaches 66% at a sweep rate of 0.2 mV s^{-1}. And it increases gradually with the increase in sweep rate and reaches 90.24% at 1 mV s^{-1} (Fig. 5d). This is mainly attributed to the fact that high scan speeds usually cause an increase in electrochemical polarization and that the zinc ions are not able to fully (de)intercalate at the corresponding electrode potentials. Fast Faraday reactions can only occur at or near the interface of the electrode material, thus leading to an increase in the proportion of capacitive contribution.[36] The reaction kinetics of the

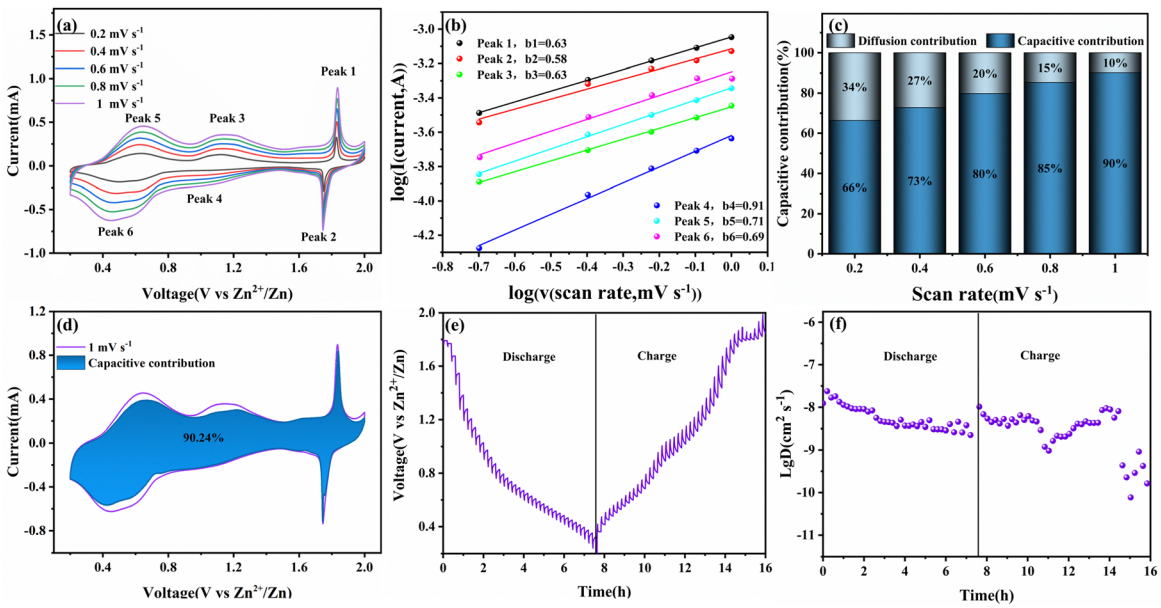

Fig. 5 (a) Multi-sweep CV curves, (b) the determination of b values through the relationship of peak current and scan rate, (c) the contributions of capacitance and diffusion, (d) capacitive contribution of CV profile at 1 mV s^{-1}, (e) GITT bright and (f) the corresponding ion diffusion coefficients for ZnVHCF@rGO.

Published on 13 February 2025. Downloaded on 1/18/2026 11:00:12 PM.

electrodes are further investigated using EIS. As shown in Fig. S7 (ESI†), the Nyquist plot demonstrates a concave semicircle in the high-frequency region and the linear portion in the low-frequency. The former is related to the charge transfer resistance (R_{ct}) and the latter is the Warburg impedance (W_o) correlated with ion diffusion.[53] Apparently, ZnVHCF@rGO has the lowest R_{ct}, indicating a smaller charge transfer impedance. Furthermore, the ion diffusion kinetics of the material is discussed using the GITT technique.[54] As shown in Fig. 5e and f, the ion-averaged diffusion coefficients (D) of ZnVHCF@rGO remained in the order of magnitude at 10^{-7} to 10^{-10}, which is higher than that of ZnVHCF (10^{-8} to 10^{-11}) as shown in Fig. S8 (ESI†). The above results demonstrate that the presence of the rGO conductive network makes the material have a low charge transfer resistance and a high diffusion coefficient of zinc ions. It can improve the material conductivity and enhance the charge transfer kinetics of ZnVHCF@rGO.

Using *ex situ* XRD, the structural evolution of ZnVHCF@rGO is investigated during charging and discharging processes and the results are shown in Fig. 6a. The strong diffraction peak at 43.4° is attributed to the stainless-steel mesh substrate. Due to the presence of diphasic Prussian blue, ZnVHCF can utilize the double backbone structure to extract/insert zinc ions. Specifically, the characteristic peak at 16.3° is attributed to the (113) crystal plane of ZnHCF. It can be noticed that the insertion of zinc ions during discharge leads to the widening of the layer spacing, and the peak essentially returns to the initial angle after full charging. ZnHCF remains in its original phase without multiphase transitions involving the disappearance of old peaks and the appearance of new peaks.[37] The insertion/extraction of Zn^{2+} only induces shifts in the peaks, leading to expansion and contraction of the ZnHCF lattice and contributing to a stable long cycle. Additionally, the peak at 24.8° in the XRD pattern belongs to the VHCF. During the first discharge, the single peak at 24.8° splits into a doublet with the insertion of zinc ions, indicating that the crystal structure of VHCF changes from a cubic phase to a rhombic phase. And the structure is maintained in the rhombic phase during charging. Compared to the pristine state, the results show that the crystal structure of VHCF changes from a cubic phase to a rhombic phase after the charging/discharging process, and then the ion insertion/extraction process is reversible in the rhombic phase.[43]

Meanwhile, the evolution of Zn, V and Fe valence states is detected using the XPS technique to further analyze the charging and discharging mechanism of ZnVHCF@rGO. Fig. 6c shows the variation of the V 2p peak in different states. When discharged to 0.2 V, the portion of V^{5+} and V^{4+} is reduced to V^{4+}

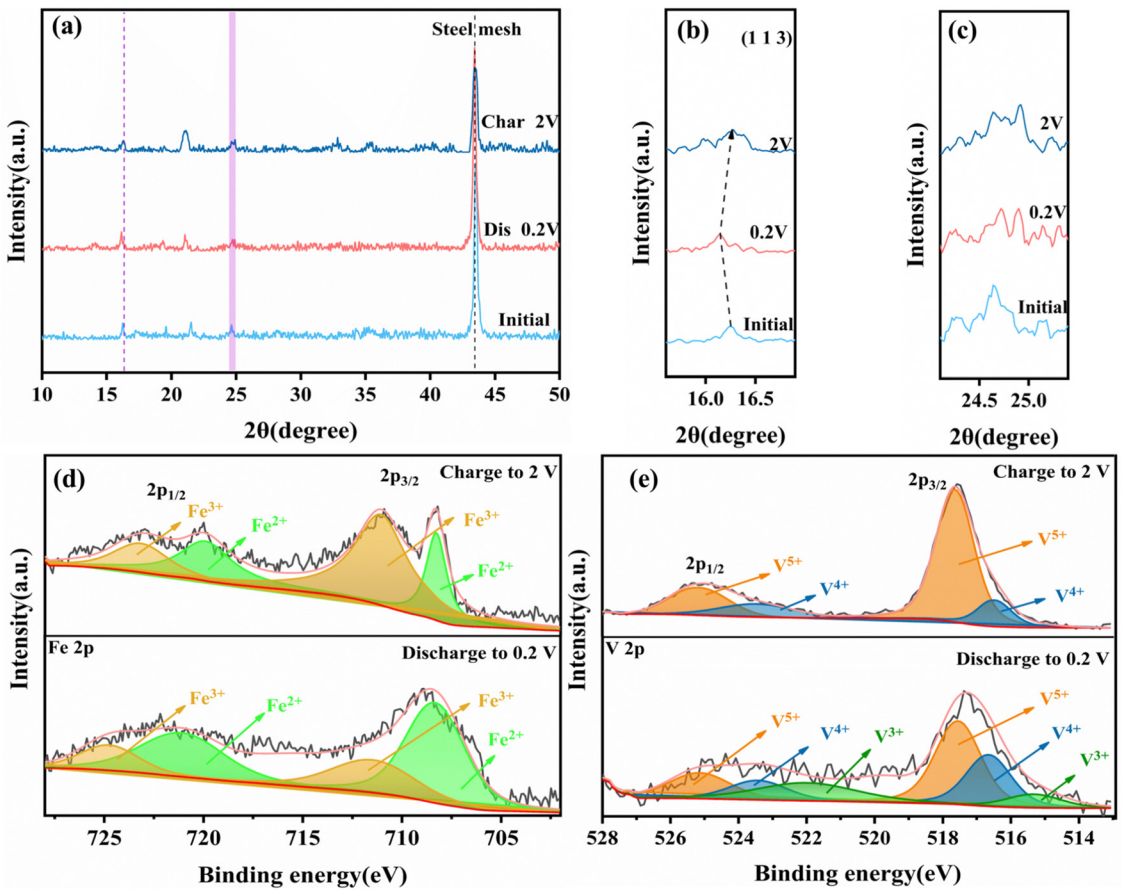

Fig. 6 (a)–(c) The corresponding XRD image of ZnVHCF@rGO during charge/discharge; XPS spectra of (d) V 2p and (e) Fe 2p during the charge/discharge process for ZnVHCF@rGO.

 This journal is © The Royal Society of Chemistry 2025

Published on 13 February 2025. Downloaded on 1/18/2026 11:00:12 PM.

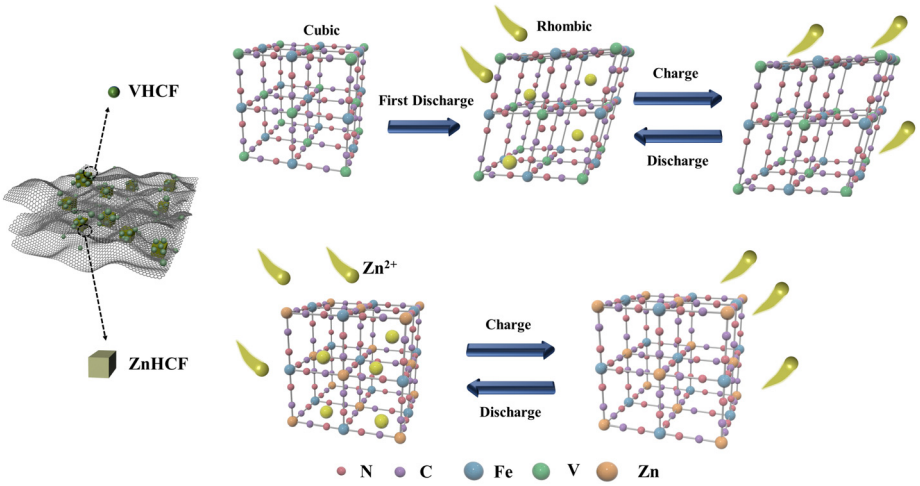

Fig. 7 The reaction mechanism of the ZnVHCF@rGO during charge/discharge.

and V^{3+} to balance the charge due to the insertion of Zn^{2+}. In contrast, when charged to 2.0 V, the V^{3+} peak disappears and the valence state of V is dominated by V^{5+} and V^{4+}. Likewise, the peak variation of Fe 2p in different states can also be observed in Fig. 6e. When discharged to 0.2 V, it presents more Fe^{2+} and when charged to 2.0 V, the Fe^{3+} signal is more pronounced. In the XPS spectra of Zn 2p (Fig. S9, ESI†), it can be observed that the intensity of the Zn peak when discharged to 0.2 V is significantly higher than that at 2.0 V, indicating the successful insertion of Zn^{2+} into the cathode material. In contrast, the intensity of the Zn peak is significantly weakened at 2.0 V, suggesting reversible insertion and extraction of Zn^{2+}. And the schematic of structural evolution and the processes of ion insertion and extraction are illustrated in Fig. 7.

4. Conclusion

In summary, a diphasic Prussian blue material enhanced by reduced graphene oxide conductive is designed in this study, and exhibits superior electrochemical performance. V and Fe enable multiple electron transfer during charging and discharging to achieve higher specific capacity. The introduction of the rGO conductive network enables fast electron transfer and ion diffusion. ZnVHCF@rGO shows a higher specific capacity of 152.3 mA h g^{-1} at 0.1 A g^{-1} and good rate capability. Meanwhile, according to the principle of dissolution equilibrium, the dissolution of the material is effectively inhibited, and the cycle stability is improved by adding the VO^{2+} electrolyte additive. Additionally, it also provides additional capacity due to the electrochemical activity of V. The multi-part synergistic effect enhances the cycling performance and energy storage capacity of ZnVHCF@rGO cathode materials (166.8 mA h g^{-1} at 0.1 A g^{-1}). And it has specific capacity of 84.1 mA h g^{-1} at 5 A g^{-1} with a capacity retention of 72.1% after 300 cycles. Finally, it was utilized to reveal the reaction mechanism and structural stability of the ZnVHCF@rGO electrode by *ex situ* characterization. This work could provide new insights for exploring effective cathode materials for aqueous zinc ion batteries based on PBAs.

Data availability

The data supporting this article have been included as part of the ESI.†

Conflicts of interest

There are no conflicts to declare.

Acknowledgements

This work was supported by the Science and Technology Research Program of Chongqing Municipal Education Commission (Grant No. KJQN202300759); the Vanadium Titanium Materials Engineering Technology Research Center Foundation Project of Sichuan (No. 2022FTGC07); the National Key R&D Program of China Grant Number (2023YFC3009500); the Campus Science Fund Project of Chongqing Jiaotong University (No. 2020020086; No. 2020023032); the Graduate Tutor Team Construction Project of Chongqing (No. JDDSTD2022006); the Graduate Student Research Innovation Project of Chongqing (No. 2024S0110).

References

1 J. H. Huang, X. Qiu, N. Wang and Y. G. Wang, *Curr. Opin. Electrochem.*, 2021, **30**, 100801.
2 L. Li, Q. C. Zhang, B. He, R. Pan, Z. Wang, M. Chen, Z. Wang, K. Yin, Y. Yao, L. Wei and L. Sun, *Adv. Mater.*, 2022, **34**, 2104327.
3 A. Mauger, C. M. Julien, A. Paolella, M. Armand and K. Zaghib, *Materials*, 2019, **12**, 3892.
4 Z. J. Zhang, M. Y. Shu, Y. Jiang and J. Xu, *Chem. Eng. J.*, 2021, **414**, 128889.

Published on 13 February 2025. Downloaded on 1/18/2026 11:00:12 PM.

5 S. C. Wang, W. W. Deng, Z. Y. Geng, P. Y. Li, N. Q. Hu, L. M. Zhu, W. Sun and C. M. Li, *Battery Energy*, 2023, **2**, 20220050.
6 N. Zhang, X. Y. Chen, M. Yu, Z. Niu, F. Cheng and J. Chen, *Chem. Soc. Rev.*, 2020, **49**, 4203–4219.
7 J. H. Huang, Z. W. Guo, Y. Y. Ma and D. Bin, *Small Methods*, 2019, **3**, 1800272.
8 S. T. Lian, Z. J. Cai, M. Y. Yan, C. L. Sun, N. Y. Chai, B. M. Zhang, K. S. Yu, M. Xu, J. X. Zhu, X. L. Pan, Y. H. Dai, J. Z. Huang, B. Mai, L. Qin, W. C. Shi, Q. Q. Xin, X. Y. Chen, K. Fu, Q. Y. An, Q. Yu, L. Zhou, W. Luo, K. N. Zhao, X. W. Wang and L. Q. Mai, *Angew. Chem., Int. Ed.*, 2024, **63**, e202406292.
9 Z. J. Cai, J. P. Wang, S. T. Lian, J. W. Chen, F. Lang, Z. Li and Q. Li, *Adv. Funct. Mater.*, 2024, 2401367.
10 X. Y. Lei, Z. P. Ma, L. Bai, L. Wang, Y. L. Ding, S. L. Song, A. L. Song, H. F. Dong, H. Tian, H. J. Tian, X. T. Meng, H. Liu, B. Sun, G. J. Shao and G. i Wang, *Battery Energy*, 2023, **2**, 20230024.
11 Z. R. Tao, J. W. Cui, Y. M. Tan, Z. Zhou, Z. Chen, A. D. Wang, Y. F. Zhu, S. M. Lai, M. H. Yu and Y. Y. Yang, *Small*, 2023, **19**, e2301620.
12 B. B. Hu, J. Jiang, P. P. Wang, H. Cheng, D. S. Li, Z. D. Zhou, Y. Deng, N. Zhao, X. Y. Yuan and Z. Li, *ACS Appl. Nano Mater.*, 2025, **8**, 720–732.
13 T. Zhou, L. M. Zhu, L. L. Xie, Q. Han, X. Yang, L. Chen, G. Wang and X. Cao, *J. Colloid Interface Sci.*, 2022, **605**, 828–850.
14 A. Q. Zhang, R. Zhao, Y. H. Wang, J. Yang, C. Wu and Y. Bai, *Energy Environ. Sci.*, 2023, **16**, 3240–3301.
15 F. Wan and Z. Q. Niu, *Angew. Chem., Int. Ed.*, 2019, **58**, 16358–16367.
16 B. B. Hu, X. Y. Yang, D. S. Li, L. Luo, J. Jiang, T. Du, H. Pu, G. Ma, B. Xiang and Z. Li, *J. Alloys Compd.*, 2024, **1008**, 176801.
17 F. Ma, Q. Li, T. Y. Wang, H. Zhang and G. Wu, *Sci. Bull.*, 2017, **62**, 358–368.
18 K. Hurlbutt, S. Wheeler, I. Capone and M. Pasta, *Joule*, 2018, **2**, 1950–1960.
19 M. Oliver-Tolentino, G. Ramos-Sánchez, G. Guzmán, M. Avila, I. González and E. Reguera, *Solid State Ionics*, 2017, **312**, 67–72.
20 B. He, P. Ma, Q. C. Zhang and C. Wang, *Small*, 2019, **15**, 1905115.
21 L. Y. Zhang, L. Chen, X. F. Zhou and Z. Liu, *Adv. Energy Mater.*, 2015, **5**, 1400930.
22 L. T. Ma, H. L. Cui, S. M. Chen, X. Li, B. Dong and C. Zhi, *Nano Energy*, 2021, **81**, 105632.
23 J. Yang, W. X. Hou, L. Q. Ye, G. Y. Hou, C. Yan and Y. Zhang, *Small*, 2023, **20**, 2305386.
24 Y. T. Xue, X. P. Shen, H. Zhou, J. Cao, J. Pu, Z. Ji, L. Kong and A. Yuan, *Chem. Eng. J.*, 2022, **448**, 137657.
25 W. C. Zhuo, J. L. Li, X. D. Li, L. Ma, G. Yan, H. Wang, S. Tan and W. Mai, *Surf. Interfaces*, 2021, **23**, 100911.
26 H. Wang, L. Wang, S. M. Chen, G. Li, J. Quan, E. Xu, L. Song and Y. Jiang, *J. Mater. Chem. A*, 2017, **5**, 3569–3577.
27 B. Mai, B. Y. Xing, Y. F. Yue, N. Y. Cai, C. C. Cai, S. T. Lian, H. Fan, M. Y. Yan, T. Zhu, P. Hu, X. W. Wang and L. Q. Mai, *J. Mater. Sci. Technol.*, 2023, **165**, 1–7.
28 G. G. Bizuneh, A. M. M. Adam and J. Ma, *Battery Energy*, 2023, **2**, 20220021.
29 H. W. Liu, N. Z. Wang, L. Hu, M. Sun, Z. Li and C. Jia, *Electrochim. Acta*, 2023, **441**, 141856.
30 P. H. Trindade Soares and E. Nossol, *ACS Appl. Nano Mater.*, 2019, **2**, 2241–2249.
31 Y. Sun, Y. L. Yang, X. L. Shi, L. Y. Ye, Y. W. Hou, J. X. Wang, G. Q. Suo, S. Y. Lu and Z. G. Chen, *Battery Energy*, 2023, **2**, 20220046.
32 J. M. Yue, L. D. Lin, L. W. Jiang, Q. Zhang, Y. Tong, L. Suo, Y.-s Hu, H. Li, X. Huang and L. Chen, *Adv. Energy Mater.*, 2020, **10**, 2000665.
33 J. H. Chen, Z. F. Yan, K. Li, A. J. Hu, B. R. Yang, T. Li, M. He, Y. J. Li, Z. Wei Seh and J. P. Long, *Battery Energy*, 2024, **3**, 20230063.
34 S. C. Liu, J. F. He, D. S. Liu, M. Ye, Y. Zhang, Y. Qin and C. C. Li, *Energy Storage Mater.*, 2022, **49**, 93–101.
35 L. S. Zhang, J. S. Hu, B. Zhang, J. Liu, H. Wan, L. Miao and J. Jiang, *J. Mater. Chem. A*, 2021, **9**, 7631–7639.
36 B. B. Hu, X. Y. Yang, D. S. Li, J. Jiang, C. Liu, Y. Deng, H. Pu, G. Ma and Z. Li, *Ceram. Int.*, 2023, **50**, 8421–8428.
37 Y. M. Tan, Z. Chen, Z. R. Tao, A. Wang, S. Lai, S. Ho and Y. Yang, *Energy Storage Mater.*, 2024, **67**, 103274.
38 J. Q. Huang, X. W. Chi, J. H. Yang and Y. Liu, *ACS Appl. Mater. Interfaces*, 2020, **12**, 17583–17591.
39 X. C. Peng, H. C. Guo, W. H. Ren, Z. Su and C. Zhao, *Chem. Commun.*, 2020, **56**, 11803–11806.
40 Q. Li, K. X. Ma, C. Hong, Z. Yang, C. Qi, G. Yang and C. Wang, *Energy Storage Mater.*, 2021, **42**, 715–722.
41 J. L. Zhan, W. Zhu, Y. S. Liu, M. Li, J. Zhao, H. Su, J. Ding, J. Sun and Y. Xu, *Adv. Funct. Mater.*, 2023, **33**, 2301935.
42 L. Li, Z. Hu, Y. Lu, C. Wang, Q. Zhang, S. Zhao, J. Peng, K. Zhang, S. L. Chou and J. Chen, *Angew. Chem., Int. Ed.*, 2021, **60**, 13050–13056.
43 Y. J. Zhang, Y. Wang, L. Lu, C. Sun and D. W. Yu, *J. Power Sources*, 2021, **484**, 229263.
44 X. Y. Dong, Z. Li, D. R. Luo, K. Huang, H. Dou and X. Zhang, *Adv. Funct. Mater.*, 2023, **33**, 2210473.
45 L. Z. Sheng, H. Jiang, S. P. Liu, M. Chen, T. Wei and Z. Fan, *J. Power Sources*, 2018, **397**, 325–333.
46 R. L. Li, W. B. Yue and X. Chen, *J. Alloys Compd.*, 2019, **784**, 800–806.
47 Z. X. Xu, W. B. Yue, R. Lin, C.-Y. Chiang and W. Zhou, *J. Energy Storage*, 2019, **21**, 647–656.
48 M. C. Biesinger, L. W. M. Lau, A. R. Gerson and R. S. C. Smart, *Appl. Surf. Sci.*, 2010, **257**, 887–898.
49 T. F. Yi, L. Y. Qiu, J. P. Qu, H. Y. Liu, J. H. Zhang and Y. R. Zhu, *Coord. Chem. Rev.*, 2021, **446**, 214124.
50 Z. X. Fan, X. Y. Liu, J. C. Qian, J. Tang, J. Yu, W. He and Z. M. Sun, *Energy Technol.*, 2022, **10**, 2200390.
51 Z. Y. Feng, Y. F. Zhang, J. J. Sun, Y. Liu, H. Jiang, M. Cui, T. Hu and C. Meng, *Chem. Eng. J.*, 2022, **433**, 133795.
52 X. J. Li, X. D. Zhu, Z. Y. Cao, Z. Xu, J. Shen and M. Ye, *Small*, 2022, **18**, 2105325.
53 Z. F. Yao, D. P. Cai, Z. X. Cui, Q. Wang and H. Zhan, *Ceram. Int.*, 2020, **46**, 11237–11245.
54 Y. X. Tong, Y. Zang, S. D. Su, Y. Zhang, J. Fang, Y. Yang, X. Li, X. Wu, F. Chen, J. Hou and M. Luo, *J. Energy Chem.*, 2023, **77**, 269–279.

 This journal is © The Royal Society of Chemistry 2025